Optimal Reduced Basis Method for Aeroacoustics with Impedance Boundary Conditions

Rémi Roncen, Philip Edel, Christophe Peyret

Optimal Reduced Basis Method for Aeroacoustics with Impedance Boundary Conditions

Rémi Roncen *
ONERA, Multi-physics department for energetics, Toulouse University, F-31055, Toulouse, France

Philip Edel †
ONERA, Information processing and systems department, Paris Saclay University, F-91123 Palaiseau, France
Sorbonne University, Paris University, CNRS, Jacques-Louis Lions Laboratory (LJLL), F-75005 Paris, France

Christophe Peyret ‡
ONERA, Aerodynamics, aeroelasticity, acoustics department, Paris Saclay University, F-92320 Châtillon, France

Solving the linearized Euler equations in the harmonic frequency domain amounts to solving a large linear system. Doing so repetitively can be costly, especially when some parameters need to be varied (e.g., the acoustic impedance of a liner), such as in optimization and impedance eduction problems. To accelerate the calculations, the equations can first be projected onto a basis of reduced dimension, only requiring a limited number of full solutions called snapshots, calculated at different impedance values. This paper is concerned with finding an optimal set of impedances allowing the greedy creation of a reduced basis that leads to the most accurate surrogate modeling in the least number of calls to the direct solver. The optimal set of impedance values is first obtained on a 2D duct configuration, and numerical verification tests are performed on a three-dimensional engine nacelle.

Keywords: acoustic liner, impedance, snapshot, greedy RBM, linearized Euler equations, optimization

Nomenclature

Abbreviations:

BC	Boundary Condition
DG	Discontinuous Galerkin
HF	High Fidelity
IL	Insertion Loss
LEE	Linearized Euler Equations
PDE	Partial Differential Equations
RB	Reduced Basis
re(), im()	Functions taking the real and imaginary part of a complex number
SPL	Sound Pressure Level

Variables:

$\boldsymbol{A_x}$, $\boldsymbol{A_y}$, $\boldsymbol{B}$, $\boldsymbol{S}$	Matrices of the LEE
α	Acoustic attenuation coefficient, dB

Presented as Paper 2022-2901 at the 28th AIAA/CEAS Aeroacoustics Conference, Southampton, UK, 14-17 June 2022
*Research scientist; remi.roncen@onera.fr (Corresponding author)
†Research scientist
‡Research scientist

c_0	Mean speed of sound, m.s^{-1}
Δ_α	Absolute difference between two values of acoustic attenuation coefficient , dB
$\overline{\Delta_\alpha^2}$	Average of Δ_α^2
Δ_p	Quality index based on the pressure residual
ϵ_p	Approximation error on the pressure
f	Frequency, Hz
γ	Ratio of specific heats
H	Height of aeroacoustic bench, m
L	Length of the liner sample, m
$\boldsymbol{i}$	Acoustic intensity
j	Complex unit number
$\underline{\underline{\tilde{\mathcal{L}}}}$, $\underline{\underline{\tilde{\mathcal{L}}}}_1$, $\underline{\underline{\tilde{\mathcal{L}}}}_2$	Discretized operators of the DG-LEE
N	Dimension of the discretized DG-LEE system
ω	Angular frequency, rad.s^{-1}
$\tilde{p}$	Acoustic pressure, Pa
p	Polynomial order of a DG cell
$\tilde{\boldsymbol{\varphi}}$	State vector of the LEE
$\tilde{\Psi}$	Acoustic quantity of interest
$\tilde{R}$	Acoustic reflection coefficient
$\underline{\tilde{r}}$	Discretized residual of the DG-LEE
$\tilde{\boldsymbol{r}}$	Residual
$\tilde{r}_u, \tilde{r}_v, \tilde{r}_p$	Velocity and pressure components of the residual
$\tilde{\rho}$	Acoustic density, kg.m^{-3}
ρ_0	Mean density, kg.m^{-3}
$\underline{S}$	Discretized source vector of the DG-LEE
$S_1,\ S_2$	Surfaces over which the acoustic intensity is evaluated, m^2
Θ	Parameter space of a liner geometry
$\tilde{\boldsymbol{u}}$	Acoustic velocity vector
$\boldsymbol{u_0}$	Mean velocity vector
U_0, V_0, W_0	Mean flow speeds in the x, y and z directions, m.s^{-1}
$\tilde{u}, \tilde{v}, \tilde{w}$	Acoustic particle velocities in the x, y and z directions, m.s^{-1}
$\underline{\underline{V_m}}$	Reduced basis matrix of size $(N \times m)$
$\tilde{v}_n$	Normal acoustic particle velocity, m.s^{-1}

$\mathcal{D}$, Ξ	Bounded sets on which the residual is evaluated
$\underline{\xi}$	POD mode of the DG-LEE
N_Ξ	Number of elements in the discrete set Ξ
x, y, z	Spatial coordinates
$\tilde{Z}$	Normalized acoustic surface impedance

I. Introduction

Despite decades of substantial improvements in noise reduction technologies [1], aircraft noise remains a significant issue for communities neighboring airports. More generally, acoustic noise is a disturbance that interferes with speech and cognitive performance [2], and an increasing interest is dedicated to noise mitigation. In aircraft, the two main sources of noise are the airframe and the engine. For the latter noise contribution, acoustic liners are typically placed within the engine nacelle.

Acoustic liners are passive sound absorption devices mounted within the walls of complex systems such as engine nacelles, jet pumps, and can also be found in wind tunnels [3]. Acoustic liners are oftentimes made of a perforated face-sheet placed over a rigidly backed cavity, but more complex configurations have been imagined to improve the liner's efficiency over an extended frequency range [4]. For the acoustic liner designer, the goal is to choose the physical properties of the different elements leading to an optimal noise reduction.

Due to the small scale of the perforations in acoustic liners, a single complete direct numerical investigation of the liner's efficiency would be too computationally expensive for industrial applications. Full scale optimization problems are out of reach. Fortunately, a different approach can be used, consisting in representing acoustic liners as a homogenized boundary condition (BC), using the concept of surface impedance. Assuming that the liner can be treated macroscopically and that it is locally reacting, i.e., no acoustic wave propagation in the transverse direction, the surface impedance $\tilde{Z}$ is defined in the frequency domain as the ratio of the acoustic pressure $\tilde{p}$ and the normal acoustic particle velocity $\tilde{v}_n$ at a liner surface. The impedance, obtained experimentally or as a function of the liner's geometric properties [5, 6], fully characterizes the acoustic behavior of the liner.

For the acoustic liner designer, the main task is to select the geometrical properties of the liner that best meet the noise cancellation requirements, i.e., a target noise reduction for a given frequency range at a certain flight condition, while satisfying some integration constraints (total thickness, weight, surface porosity, etc.). To do so, the system (engine nacelle, duct, wind tunnel) can first be characterized numerically at all frequencies of interest, for a large range of impedance values that potential liner candidates could attain. Following this large series of direct calculations, acoustic quantities of interest can be mapped onto the impedance real and imaginary parts. One can then test different liner models, changing their geometric properties to evaluate their impedance, and use the impedance map to evaluate acoustic quantities. For large systems, where the cost of a high-fidelity (HF) calculation is important, the creation of such impedance maps can become intractable.

The second task that arises in aeroacoustic problems involving liners is that of impedance *eduction*: using experimental data retrieved in an aeroacoustic duct, one can indirectly measure the liner's impedance via its influence on the acoustic field [7–14], by solving an inverse problem. This experimental-numerical step is all the more important because liner impedance has been shown to depend on the grazing flow profile [15–17], the sound pressure level (SPL) [15, 18, 19], and even the direction of the propagating waves [20–25]. This eduction process often requires an accurate numerical model, and many solver evaluations. Due to the influence of the flow on the educed impedance value, there is a potential interest in using fully 3D calculations in impedance eduction with resolved flow profiles, instead of 2D calculations that oftentimes use a uniform flow profile. Adding a dimension to the problem is bound to slow down all the eduction codes, and a faster approach is required.

Reduced order models (ROM) are thus necessary for problems of practical interest, where the system complexity has to be reduced. Model order reduction is a well-known approach to relieve the computational burden associated with numerous HF computations for a vast set of parameter values. It consists in replacing the costly HF solver by a ROM featuring much fewer degrees of freedom [26]. Properly built, a ROM is able to approximate the HF solution for any parameter value at very low cost and with high accuracy. In the context of noise cancellation in large systems, one could benefit from such a model reduction when performing the optimization of the properties of an acoustic liner, for instance. The approach followed in this work to reduce the computational effort is the reduced basis (RB) method. In

this method, the HF solution at any parameter value is approximated by a linear combination of a small number of HF solutions computed for a small set of parameter values [27]. The RB method has been successfully applied in acoustics to the parametrized Helmholtz equation (see e.g. [28, 29]). To the best of our knowledge, Ref. [13] was the first to apply the RB method in the context of impedance-parametrized linearized Euler equations (LEE). The authors reported a speed-up factor of the order of 10^3, which was obtained at the price of 30 calls to the HF solver, where the impedance was randomly sampled to generate the basis.

The main novelty of the present work, compared with that of Ref. [13], is the use of a *greedy* sampling strategy in order to minimize the number of calls to the HF solver [27, 30, 31]. We address the critical question of the selection of snapshots, i.e., how to choose the impedance values at which the direct solver needs to be evaluated? A numerical investigation is set up to show the benefits of the greedy approach, which uses a particular indicator to iteratively select the optimal impedance values.

The aeroacoustic problem is first recalled in Sec. II, and a Discontinuous-Galerkin (DG) harmonic solver is presented to solve the LEE with an impedance BC in the frequency domain. In Sec. III, the RB technique is detailed. The crux of the problem is addressed in Sec. III, where the residual-driven greedy approach is detailed. In Sec. IV, the technique is applied on a 2D duct configuration to obtain an optimal set of impedance values, and different cases are explored. This optimal set is then tested in a fully 3D configuration of an engine nacelle in Sec. V to evaluate the generalizability of the optimal set of impedance values. Conclusions are drawn in Sec. VI.

II. High-fidelity solver

This section deals with the introduction of the HF solver, relying on a high-order numerical scheme that discretizes the LEE onto a mesh. The 2D duct configuration used for numerical validation purposes is presented, as well as the general strategy allowing one to only create the system matrices once.

The direct problem consists in numerically calculating the acoustic fields (pressure and velocity) in a grazing flow duct, in the presence of a liner. A locally reacting liner is classically represented by an impedance BC. The 2D LEE are solved using a harmonic DG scheme [11, 13], succinctly recalled here for completeness.

A small scale aeroacoustic bench is considered for the present numerical investigations. A schematic of ONERA's B2A bench is shown in Fig. 1, along with the area where measurements can be performed (microphone measurements on the wall opposite the liner). An example of the 2D numerical mesh is also given (done in Gmsh [32]). The liner is located at the bottom wall ($y = 0$) and has a length of $L = 150\,\text{mm}$. The duct cross-section is square with a size of $H = 50\,\text{mm}$.

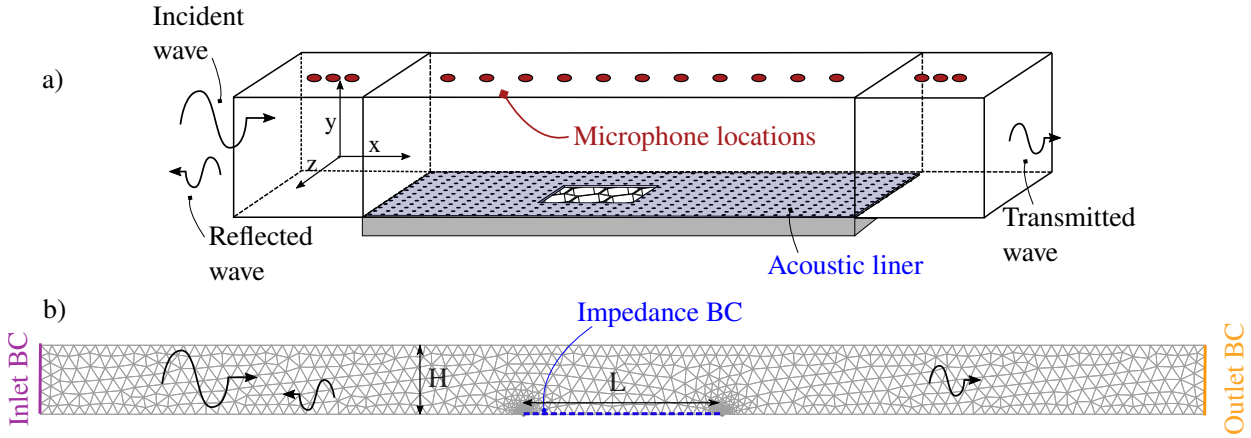

Figure 1 a) Schematic of the B2A aeroacoustic bench; b) Schematic of the mesh used.

The method description presented in this section is mostly inherited from previous work in Ref. [13, II.B], with the distinction that the current solver does not use an hypothesis of constant ambient speed of sound and density to simplify the equations, hence the difference in the $\boldsymbol{B}$ matrix. The 2D simulations are carried out in the (x, y) plane at the center of the duct span (see Fig. 1).

The LEE, written in non-conservative form with an $e^{j\omega t}$ time dependence ($\omega = 2\pi f$, with f the frequency in Hz)

are given by

$$\mathrm{j}\omega\tilde{\boldsymbol{\varphi}} + \boldsymbol{A_x}\partial_x\tilde{\boldsymbol{\varphi}} + \boldsymbol{A_y}\partial_y\tilde{\boldsymbol{\varphi}} + \boldsymbol{B}\tilde{\boldsymbol{\varphi}} = \boldsymbol{S}, \tag{1}$$

where j is the complex unit, $\tilde{\boldsymbol{\varphi}}$ is the state vector with the tilda mark $\tilde{\cdot}$ denoting a frequency dependent quantity, $\boldsymbol{A_x}$, $\boldsymbol{A_y}$, $\boldsymbol{B}$ are flux matrices of size $\mathbb{R}^{3\times3}$, and $\boldsymbol{S}$ is a source vector injecting waves in the domain. The matrices read

$$\boldsymbol{A_x} = \begin{pmatrix} U_0 & 0 & c_0 \\ 0 & U_0 & 0 \\ c_0 & 0 & U_0 \end{pmatrix},\ \boldsymbol{A_y} = \begin{pmatrix} V_0 & 0 & 0 \\ 0 & V_0 & c_0 \\ 0 & c_0 & V_0 \end{pmatrix},\ \boldsymbol{B} = \begin{pmatrix} \partial_x U_0 & \partial_y U_0 & \partial_x c_0 \\ \partial_x V_0 & \partial_y V_0 & \partial_y c_0 \\ \frac{c_0}{\rho_0}\partial_x\rho_0 & \frac{c_0}{\rho_0}\partial_y\rho_0 & \frac{\gamma-1}{2}\left(\partial_x U_0 + \partial_y V_0\right) \end{pmatrix}. \tag{2}$$

In Eq. 2, U_0 and V_0 are the x and y components of the mean flow velocity, ρ_0 is the ambient fluid density, c_0 the ambient fluid speed of sound, and γ is the heat capacity ratio. Throughout the text, the 0 subscript denotes a mean flow quantity. Components of the state vector $\tilde{\boldsymbol{\varphi}} = \left(\tilde{u}, \tilde{v}, \frac{\tilde{p}}{\rho_0 c_0}\right)$ represent the acoustic perturbations around the mean flow, with $\tilde{u}, \tilde{v}$ the x and y acoustic velocities, and $\tilde{p}$ the acoustic pressure. The present study is restricted to an incompressible mean flow. Due to the homentropy condition, the energy equation is replaced by the state equation $\tilde{p} = c_0^2\tilde{\rho}$, with $\tilde{\rho}$ the density perturbation around the mean flow density ρ_0.

A shear mean flow profile with a null mean flow velocity at the walls is considered, so the impedance BC writes

$$\tilde{p} = \rho_0 c_0 \tilde{Z}\tilde{v}_n, \tag{3}$$

where $\tilde{v}_n$ is the normal component of the acoustic velocity (pointing into the liner, thus equal to $-\tilde{v}|_{y=0}$ in the present case). The impedance $\tilde{Z}$ is normalized by $\rho_0 c_0$ in this work. It is unpractical to work directly with the impedance, since the quantity is unbounded. In Refs. [33, 34], it was shown to be more efficient to consider instead the reflection coefficient $\tilde{R}$, defined by

$$\tilde{R} = \frac{\tilde{Z} - 1}{\tilde{Z} + 1}, \quad \tilde{R} \in \mathbb{C}, \left|\tilde{R}\right| \leq 1. \tag{4}$$

In the remainder of this study, the reflection coefficient is used to represent an impedance BC.

A DG scheme is chosen to solve Eq. 1 and the associated BCs. Discontinuities are allowed at the interface between two elements, and the communication between elements is enforced via a numerical flux. Let us denote N the number of degrees of freedom which depends on the number of mesh elements (in the 2D case, $\sim 10^3 - 10^4$) and the DG order (here $p = 2$). In this situation, the discretization of Eq. 1 is

$$\underline{\underline{\tilde{\mathcal{L}}}}\left(\tilde{R}\right)\underline{\tilde{\varphi}}\left(\tilde{R}\right) = \underline{S}, \tag{5}$$

where a single underbar denotes an array element of size N, while a double underbar denotes a matrix of size $N \times N$. $\underline{\underline{\tilde{\mathcal{L}}}}\left(\tilde{R}\right)$ is a complex, non-hermitian and $\tilde{R}$-dependent matrix, and $\underline{\tilde{\varphi}}\left(\tilde{R}\right) \in \mathbb{C}^N$ denotes the $\tilde{R}$-dependent numerical approximation of acoustic pressure and velocity fields. Note that the source represented by $\underline{S} \in \mathbb{C}^N$ does not depend on the reflection coefficient. It is to be noted that the matrix $\underline{\underline{\tilde{\mathcal{L}}}}\left(\tilde{R}\right)$ has an explicit dependency in $\tilde{R}$, since one can write $\underline{\underline{\tilde{\mathcal{L}}}}\left(\tilde{R}\right) = \underline{\underline{\tilde{\mathcal{L}}}}_1 + \tilde{R}\underline{\underline{\tilde{\mathcal{L}}}}_2$, where $\underline{\underline{\tilde{\mathcal{L}}}}_1$ and $\underline{\underline{\tilde{\mathcal{L}}}}_2$ are two complex $\tilde{R}$-independent $N \times N$ matrices. This linear relationship comes from the flux matrix of the reflection BC, as shown in [13, Eq. 4]*. As a result of this linear dependency, one only has to create $\underline{\underline{\tilde{\mathcal{L}}}}_1$ and $\underline{\underline{\tilde{\mathcal{L}}}}_2$ once, avoiding their potentially costly assembly each time one changes the value of $\tilde{R}$.

The DG method can handle discontinuities at hard-soft wall interfaces using numerical fluxes [11, 35–37]. These fluxed properly enforce communication between neighboring cells, and with the BCs. The DG method stability was shown in Ref. [38]. To avoid aliasing errors that could cause instabilities when a shear grazing flow is present, high order quadrature rules are used (see e.g., Ref. [39, Sec. 5.3]).

III. Reduced basis approach

Solving the partial differential equations (PDEs) described by Eq. 1 repetitively would be prohibitively long, especially when a large number of frequencies and different Mach numbers are considered to design a liner that is optimal in a wide range of conditions. Without any acceleration, a single evaluation of the PDEs takes about a second in a simple 2D configuration, at one frequency/flow profile. A *quantity of interest* $\tilde{\Psi}\left(\tilde{R}\right)$ can then be derived from the knowledge of the acoustic fields, and could be for example the insertion loss (IL†) of the system to be optimized. While

*Note that in Ref. [13], we used the notation β instead of $\tilde{R}$.

†The IL is typically defined as the difference between the SPL of a rigid case configuration and the SPL of a lined configuration, in . High values of IL correspond to efficient liners.

it may seem fast, doing N_{eval} function evaluations could still easily require over an hour without acceleration, for each frequency/Mach number. In an optimization problem, the number of required evaluation depends on the complexity of the liner geometry, represented by its parameter space Θ: $\tilde{R} = \tilde{R}(\Theta)$. Instead of performing an optimization directly on Θ, i.e., optimizing $\tilde{\Psi}\left(\tilde{R}(\Theta)\right)$, it is much more efficient to split the problem into two sub-problems, due to the time-scale disparity between the calculations of $\tilde{R}(\Theta)$ and $\tilde{\Psi}\left(\tilde{R}\right)$. As discussed in the introduction, impedance maps of acoustic quantities need only be created once (or rather, reflection coefficient maps), i.e., the calculation of $\tilde{\Psi}\left(\tilde{R}\right)$ can be done offline to cover a large number of reflection coefficient values in the unit complex circle. Then, an interpolation tool can be used to return $\tilde{\Psi}\left(\tilde{R}\right)$ for all possible values of $\tilde{R}$, at minimal cost. This map-building step is the numerically intensive operation dominating the cost of the optimization, since calculating $\tilde{R}(\Theta)$ is usually instantaneous on current machines. Another advantage of this problem splitting approach is that one does not have to restart the problem from scratch when attempting the optimization of another type of liner, since the reflection coefficient maps of the observation operator can be reused.

To shorten the time-intensive operations described above, an efficient representation of the discretized state of the system $\tilde{\underline{\varphi}}$ is obtained at a lower cost by first building a reduced basis using the method of snapshots, as explained in Pinnau [40] and used for Bayesian inference in the context of liner impedance eduction in Ref. [13]. The approach is summarized again here for completeness.

The full discretized DG system (Eq. 5) is parameterized by the unknown parameters, here the reflection coefficient $\tilde{R}$. A set of n parameter samples $\left\{\tilde{R}^{(1)}, \ldots, \tilde{R}^{(n)}\right\}$ is generated (i.e., n different complex values of the reflection coefficient are picked), yielding the associated system states, or snapshots: $\left\{\tilde{\underline{\varphi}}^{(1)}, \ldots, \tilde{\underline{\varphi}}^{(n)}\right\}$. Following standard proper orthogonal decomposition (POD) practice [40], a singular value analysis is performed to extract the $m < n$ dominant modes $\left\{\underline{\xi}^{(1)}, \ldots, \underline{\xi}^{(m)}\right\}$ and a reduced basis is defined as $\underline{\underline{V_m}} = \left[\underline{\xi}^{(1)} \,|\, \cdots \,|\, \underline{\xi}^{(m)}\right] \in \mathbb{C}^{N \times m}$. Approximating Eq. 1 by a Galerkin projection yields

$$\underline{\underline{V_m}}^* \, \underline{\underline{\tilde{\mathcal{L}}}}\left(\tilde{R}\right) \underline{\underline{V_m}} \, \underline{\tilde{\varphi}_m}\left(\tilde{R}\right) = \underline{\underline{V_m}}^* \, \underline{S}, \tag{6}$$

where * stands for the conjugate transpose. The solution $\underline{\tilde{\varphi}_m}\left(\tilde{R}\right) \in \mathbb{C}^m$ of Eq. 6 is obtained via inversion of the $m \times m$ matrix $\underline{\underline{V_m}}^* \, \underline{\underline{\tilde{\mathcal{L}}}}\left(\tilde{R}\right) \underline{\underline{V_m}}$. The latter matrix can be efficiently assembled for any value of $\tilde{R}$ once the two $\tilde{R}$-independent $m \times m$ matrices $\underline{\underline{V_m}}^* \, \underline{\underline{\tilde{\mathcal{L}}}}_1 \, \underline{\underline{V_m}}$ and $\underline{\underline{V_m}}^* \, \underline{\underline{\tilde{\mathcal{L}}}}_2 \, \underline{\underline{V_m}}$ have been precomputed, thanks to the explicit dependency of $\underline{\underline{\tilde{\mathcal{L}}}}\left(\tilde{R}\right)$ in the reflection coefficient $\tilde{R}$. This allows the approximation of the state $\tilde{\underline{\varphi}}$ by a linear combination of vector elements of $\underline{\underline{V_m}}$ as

$$\tilde{\underline{\varphi}}\left(\tilde{R}\right) \approx \underline{\underline{V_m}} \, \underline{\tilde{\varphi}_m}\left(\tilde{R}\right). \tag{7}$$

When the decay of the singular values is fast, one may retain only a small number m of POD modes, which enables $m \ll N$ and so the reduced system represented by Eq. 6 is much faster to solve than the full system, while maintaining a high level of accuracy.

The main issue with POD is that the set $\left\{\tilde{R}^{(1)}, \ldots, \tilde{R}^{(n)}\right\}$ must be sufficiently large for $\left\{\tilde{\underline{\varphi}}^{(1)}, \ldots, \tilde{\underline{\varphi}}^{(n)}\right\}$, the n snapshot solutions, to adequately account for the parametric variations. In practice, this amounts to computing a large number n of HF solutions, when at the end, only a small number $m < n$ of modes are retained for the reduced basis. This limitation is tackled in Section III.

Residual-driven greedy selection

The greedy RBM presented in this Section circumvents the issue of needing a high number of snapshots, by iteratively selecting the reflection coefficient values $\left\{\tilde{R}^{(1)}, \ldots, \tilde{R}^{(n)}\right\}$ at which HF solutions are required, maintaining their number n optimally low. All computed snapshot solutions $\left\{\tilde{\underline{\varphi}}^{(1)}, \ldots, \tilde{\underline{\varphi}}^{(n)}\right\}$ are kept in the reduced basis, which corresponds to $m = n$, so the process does not require singular value analysis.

Let us define the RB residual $\tilde{\underline{r}}$, given a RB space $\underline{\underline{V_m}}$ of size m, as

$$\tilde{\underline{r}} = \underline{\underline{\tilde{\mathcal{L}}}}\left(\tilde{R}\right) \underline{\underline{V_m}} \, \underline{\tilde{\varphi}_m}\left(\tilde{R}\right) - \underline{S}, \tag{8}$$

where $\underline{\tilde{\varphi}_m}$ solves Eq. 1. Similarly to the state variable, which has three components $\tilde{\boldsymbol{\varphi}} = \left(\tilde{u}, \tilde{v}, \frac{\tilde{p}}{\rho_0 c_0}\right)$ leading to the DG-LEE state variable $\tilde{\underline{\varphi}} \in \mathbb{C}^N$, we note $\tilde{\boldsymbol{r}} = \left(\tilde{r}_u, \tilde{r}_v, \tilde{r}_p\right)$, leading to the discretized state representation in $\tilde{\underline{r}} \in \mathbb{C}^{3 \times N_w}$,

with N_w the number of degrees of freedom on the wall opposite the liner, where the pressure has been extracted to evaluate the residual. In this numerical investigation, the focus is placed on the pressure component $\underline{\tilde{r}_p} \in \mathbb{C}^{N_w}$ of the residual, extracted from $\underline{\tilde{r}}$, which in fact depends on both the reflection coefficient value $\tilde{R}$ and the RB space $\underline{\underline{V_m}}$, i.e., $\underline{\tilde{r}_p} = \underline{\tilde{r}_p}\left(\tilde{R}, \underline{\underline{V_m}}\right)$. The reflection coefficient $\tilde{R}$ takes values in some compact set $\mathcal{D} \subset \mathbb{C}$. It is proposed to measure the *quality* Δ_p of a given RB space $\underline{\underline{V_m}}$ in terms of the maximum pressure residual over the compact set $\mathcal{D} \subset \mathbb{C}$, that is

$$\Delta_p\left(\underline{\underline{V_m}}\right) = \frac{\max\limits_{\tilde{R}\in\mathcal{D}} \left\|\underline{\tilde{r}_p}\left(\tilde{R}, \underline{\underline{V_m}}\right)\right\|_2}{p_{\text{in}}}, \tag{9}$$

where p_{in} is the amplitude of the incident pressure wave, and with a low value of Δ_p indicating a high quality of the approximation. To perform the maximization in Eq. 9, the global optimization algorithm pyMOO is selected [41]. The residual norm for any reflection coefficient value is inexpensive to compute, owing to the affine dependency in $\tilde{R}$ satisfied by the operator $\underline{\underline{\tilde{\mathcal{L}}}}\left(\tilde{R}\right)$, allowing the efficient offline/online decoupling of the computational effort in the RB method [27].

There are two selection strategies that were explored to select the snapshots:

▷ random selection of the reflection coefficients, followed by POD,

▷ residual-driven greedy selection [30, 31].

This last strategy consists in the following. First, the HF solution $\underline{\varphi}^{(1)}$ obtained by solving Eq. 5 at some initial reflection coefficient value $\tilde{R}^{(1)} \in \mathcal{D}$ is computed and the RB is initialized to $\underline{\underline{V_1}} = \underline{\varphi}^{(1)}$. Here, the value selected for the initialization is $\tilde{R} = -0.998$, which corresponds to $\tilde{Z} = 10^{-3}$. The reason for this choice will be detailed in Sec. IV.A.

Then, for $n \geqslant 2$, the algorithm is updated by finding

$$\tilde{R}^{(n)} = \underset{\tilde{R}\in\mathcal{D}}{\text{argmax}} \left\|\tilde{r}_p\left(\tilde{R}, \underline{\underline{V_{n-1}}}\right)\right\|_2, \tag{10}$$

where the arg max operator selected the value of $\tilde{R}$ that maximizes $\left\|\tilde{r}_p\left(\tilde{R}, \underline{\underline{V_{n-1}}}\right)\right\|_2$. Then, the HF solution $\underline{\tilde{\varphi}}^{(n)}$ is obtained by solving Eq. 5 at this reflection coefficient value, and the RB space is updated via the concatenation of $\underline{\underline{V_{n-1}}}$ and $\underline{\tilde{\varphi}}^{(n)}$:

$$\underline{\underline{V_n}} = \left[\underline{\underline{V_{n-1}}}, \underline{\tilde{\varphi}}^{(n)}\right]. \tag{11}$$

The iterations may be stopped once the quality indicator $\Delta_p\left(\underline{\underline{V_n}}\right)$ has reached a prescribed tolerance. Notice from Eq. 10 that the RB is successively enriched with solutions at reflection coefficient values leading to the worst (i.e., the highest) residual. An intuitive rationale behind this choice is that the approximation error and the residual are positively correlated, meaning that reducing one amounts to reducing the other (this is checked a posteriori in Sec. IV.C). Our goal is to minimize the approximation error, and thus the residual. To do so, we elected to build the RB by selecting the value of reflection coefficient that maximizes the residual (hence, the error) of the current iteration of the RB, in an attempt to improve the approximation of the next iteration of the RB in this region of high error. The mathematical rationale for the success of this greedy selection strategy can be found in the works of Binev et al. [30] and Buffa et al. [31].

IV. Exploration of the greedy selection method for an aeroacoustic problem

This Section deals with the analysis of the greedy-RB method for aeroacoustic problems. In Sec. IV.A, a first example of a 2D duct without flow is considered at 500 Hz, with a single wave-inlet sending a plane wave, grazing over a liner of 15 cm. The configuration matches the experimental bench B2A available at ONERA, and was used in Ref. [13]. Noticing that the minimal value of the real part of the impedance, coined resistance, can be an important factor contributing to the quality of the resulting RB, Sec. IV.B deals with a constrained greedy-RB where a minimal value of the resistance is selected. From an experimental standpoint, the results are interesting to liner designers, especially in typical aeronautical conditions with high speed flows and SPL, which often result in high values of the resistance. In Sec. IV.D, the configuration is first complexified by considering two consecutive and distinct impedance BCs (each of

length 7.5 cm), still at 500 Hz, and the greedy-RB approach is applied with two different impedance values to optimize. In Sec. IV.E, a different 2D duct is considered, with two wave-inlets at a frequency of 2 kHz, leading to non-plane waves in the computational domain. A flow is also present, with a maximum Mach number of 0.3 at the centerline.

A. Aeroacoustic 2D duct

To illustrate the interest of the greedy selection algorithm, the 2D duct geometry defined in Sec. II is first considered. A plane wave at a frequency set to 500 Hz is imposed at the inlet. The mean velocity profile is taken constant and equal to 0 everywhere. The 2 snapshot selection strategies are tested, namely "random" and "greedy". The random strategy is repeated 50 times, each time with a new set of snapshots.

A user might not always be interested in the full solution of the problem. In practice, the solution sometimes only needs to be accurate at the microphone locations where the experimental data is obtained, i.e., where the quantity of interest Ψ is defined. As such, two different residuals can be considered: one where the full pressure field is used to calculate the maximum residual, and one where only the pressure on the wall opposite the liner is used. Since the results were similar in trend [‡], the analysis is only performed with the residual calculated on the opposite wall pressure. The convergence analyses of the maximum residual over the domain $\mathcal{D} = \left\{\tilde{R} \in \mathbb{C},\ \left|\tilde{R}\right| \leq 1\right\}$ for the two snapshot-selection strategies are displayed in Fig. 2, along with the location of said snapshots. Note that in the case of the random strategy, the maximum residual is evaluated a posteriori for comparison purposes, but is not used to update the RB, as opposed to the greedy approach. The best set of snapshots obtained in the random strategy, leading to the lowest residual, is displayed with cross markers in Fig. 2, while the remaining values of reflection coefficients and residuals are in gray.

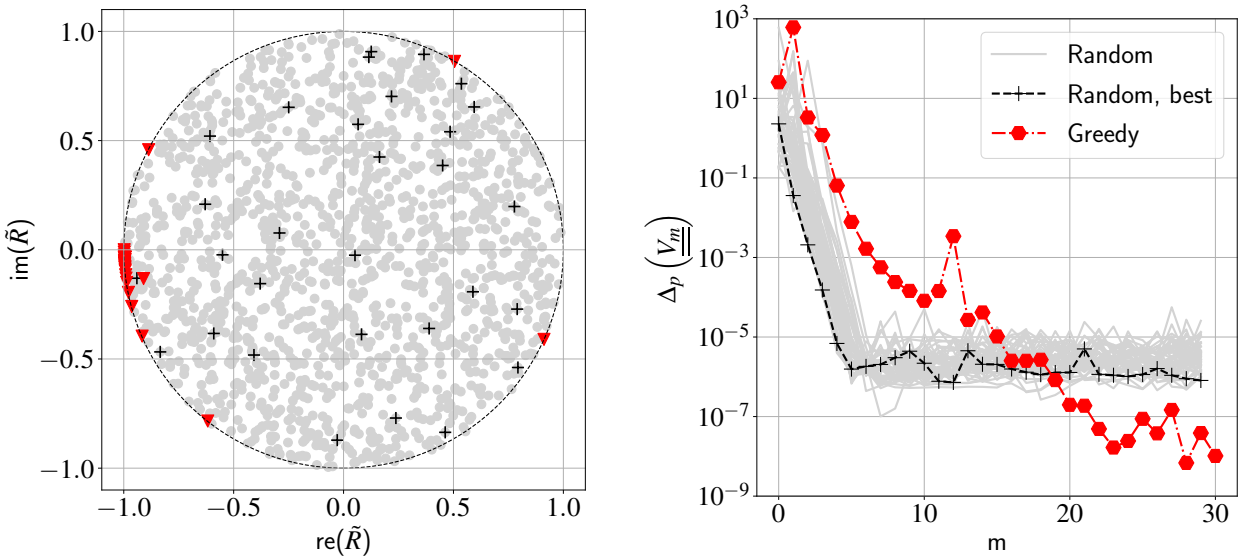

(a) Location of the snapshots in the reflection coefficient space.

(b) Diminution of the maximum residual as the number of snapshots increases.

Figure 2 Analysis of the snapshot-RB convergence. Only the pressure field on the wall opposite the liner is used to calculate the maximum residual.

Compared with the random strategy, the residual-driven greedy selection leads to an improved RB after a few iterations, as shown in Fig. 2b. As stated previously, when only the upper wall pressure is considered, the maximum residual is lower than when the entire pressure field is considered. The associated results, which are not shown for conciseness, gave very similar trends in both the locations of the snapshot and the residuals. When considering the entire domain to evaluate the residual, as opposed to only the upper wall, a high residual is located near the impedance discontinuities. Indeed, near an impedance discontinuity, a strong variation of the velocity fields, and, to a lower extent, the pressure field, is observed: the vertical component of the velocity field is discontinuous. This local "feature" seems difficult to encompass in the projection strategy of the snapshot approach, thus leading to a high residual. Interestingly,

[‡]The residual is lower when only the opposite wall is considered, as expected since it represents a subset of the total solution

the snapshot locations, i.e., the reflection coefficients used to create the snapshots, tend to cluster near $\tilde{R} = -1$ in Fig. 2a. This corresponds to impedance values close to $\tilde{Z} = 0$, associated with the largest possible impedance discontinuity. Numerically speaking, the treatment of $\tilde{Z} = 0$ is delicate, since it leads to an infinite normal velocity $\tilde{v}_n$ at the liner BC [§], and $\tilde{v}_n = 0$ at the wall BC. Numerical dissipation naturally occurs and smooths this velocity discontinuity, but no mesh convergence can be obtained. Indeed, refining the mesh locally leads to less dissipation, and a higher peak of velocity. It has to be noted that physically, passive acoustic liners cannot exactly have $\tilde{Z} = 0$ due to the presence of viscous effects. As a result, we arbitrarily enforced a lower bound to the resistance, as $\mathrm{re}\left(\tilde{Z}\right) \geq 10^{-3}$ in the numerical analysis that led to Fig. 2. The effect of the choice of this lower bound is more closely studied in Sec. IV.B. The clustering of snapshots near $\tilde{R} = -1$ validates a posteriori the choice of initial value, $\tilde{Z} = 10^{-3}$ in this case, since it is where the residual is the highest. In the initial study leading to this work [42], the initial snapshot was evaluated at $\tilde{R} = 0$ ($\tilde{Z} = 1$) due to the relative importance of this value to acousticians, since at normal incidence this represents a total absorption. While the trend for the location of snapshots was similar, the snapshot calculated at $\tilde{R} = 0$ might be wasted numerical resource in terms of convergence of the greedy algorithm in this case.

B. Constrained greedy selection of the snapshots

In this section, an attempt is made at determining a set of reflection coefficient values that are optimal for a subset of problems, where the resistance is known in advance to be larger than 0. Indeed, in aeroacoustic problems, the acoustic liner is subject to a shear grazing flow, which in turn changes the impedance value. In most impedance models [15–17], this change is mostly reflected on the real part of the impedance, where an increase is observed. In the presence of a high SPL, models also tend to yield an increase in the resistance [15, 18, 19]. As a result, the liner designer might know in advance, for a given application (engine nacelle, jet pump), the minimal value of the resistance.

The greedy strategy for snapshot selection is thus re-used, but only on the subset of reflection coefficient values corresponding to a given minimal resistance value (a constrained global optimization is performed). Following the reasoning in Sec. IV.A, the initial snapshot is evaluated at $\tilde{Z} = \min\left(\mathrm{re}\left(\tilde{Z}\right)\right)$, which corresponds to the "worst case" in terms of residual (this was verified a posteriori by changing the initial snapshot). Different minimal values are considered. The frequency of the input plane wave is set once again to 500 Hz, and a null mean flow is considered. The corresponding greedy-optimal selected reflection coefficients and impedance values are displayed in Fig. 3, and the corresponding decrease of the residual is shown in Fig. 4.

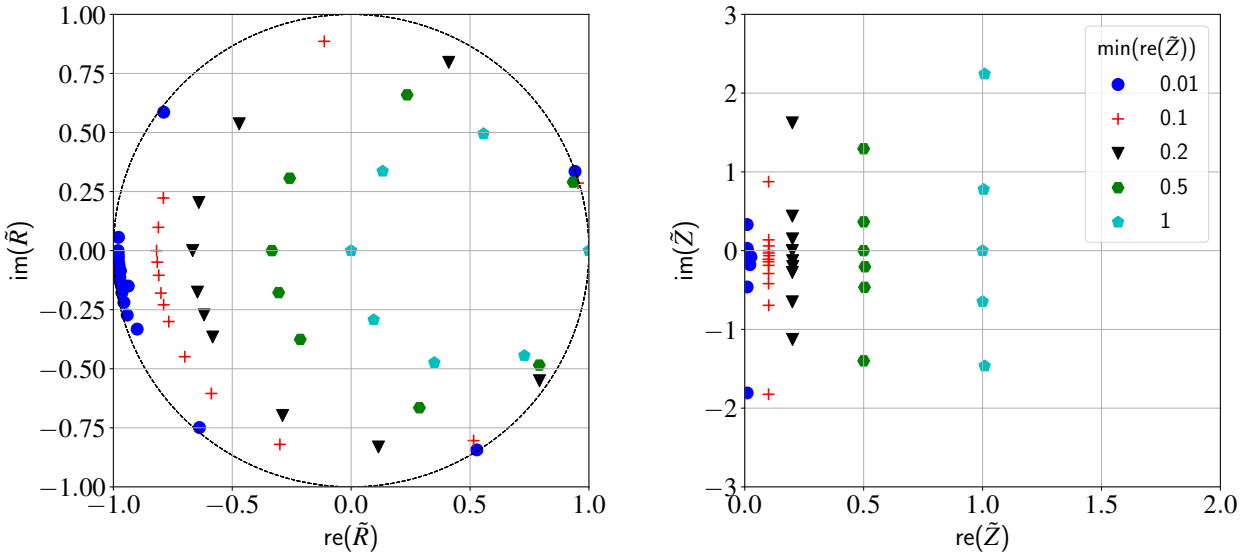

(a) Location of the snapshots in the reflection coefficient space.

(b) Location of the snapshots in a section of the impedance space.

Figure 3 Location of the optimal snapshots, for different minimal values of the resistance.

[§]Note that at normal incidence of an acoustic wave, one would have $\tilde{p} = 0$ and thus avoid the problem.

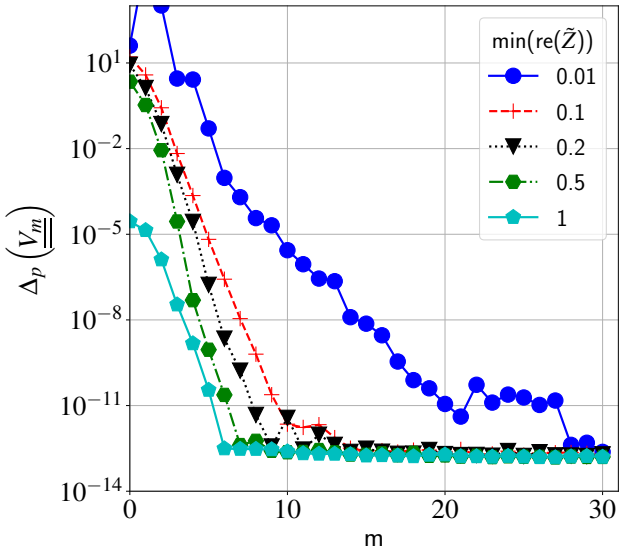

Figure 4 Diminution of the maximum residual as the number of snapshot increases.

Note that in Fig. 3, the reflection coefficient values that do not further improve the residue are not displayed, for improved readability. As the minimum of resistance re $\left(\tilde{Z}\right)$ is increased, the convergence of the maximum residual value is faster (only 7 iterations of the greedy selection are necessary when re $\left(\tilde{Z}\right) > 1$). This was expected, since the impedance discontinuity is not as marked when re $\left(\tilde{Z}\right) > 1$, meaning the pressure field features are smoother and thus easier to be projected onto a linear basis. In all cases, the greedy algorithm seems to converge close to the imposed constraint on the resistance value. Table 1 regroups the different values of reflection coefficient and impedance, in "chronological" order, in terms of building the reduced basis.

Table 1 Optimally selected values of the reflection coefficient, for different minimal values of the resistance.

$\min\left(\mathrm{re}\left(\tilde{Z}\right)\right)$	0.01		0.1		0.2		0.5		1	
m	$\mathrm{re}\left(\tilde{R}^i\right)$	$\mathrm{im}\left(\tilde{R}^i\right)$	$\mathrm{re}\left(\tilde{R}^i\right)$	$\mathrm{im}\left(\tilde{R}^i\right)$	$\mathrm{re}\left(\tilde{R}^i\right)$	$\mathrm{im}\left(\tilde{R}^i\right)$	$\mathrm{re}\left(\tilde{R}^i\right)$	$\mathrm{im}\left(\tilde{R}^i\right)$	$\mathrm{re}\left(\tilde{R}^i\right)$	$\mathrm{im}\left(\tilde{R}^i\right)$
1	-0.980	0.000	-0.818	0.000	-0.667	0.000	-0.333	0.000	0.000	0.000
2	-0.788	0.586	-0.113	0.886	0.410	0.797	0.933	0.290	1.000	0.000
3	-0.900	-0.332	0.515	-0.804	0.792	-0.551	0.235	0.659	0.557	0.495
4	-0.937	-0.150	0.954	0.286	-0.288	-0.698	0.287	-0.665	0.350	-0.474
5	0.529	-0.843	-0.588	-0.605	-0.582	-0.366	-0.214	-0.376	0.133	0.336
6	0.942	0.335	-0.767	-0.300	-0.471	0.537	-0.258	0.307	0.095	-0.293
7	-0.638	-0.749	-0.800	-0.180	-0.646	-0.176	0.791	-0.484	0.728	-0.444
8	-0.942	-0.273	-0.790	0.223	0.115	-0.831	-0.305	-0.178		
9	-0.956	-0.219	-0.699	-0.449	-0.640	0.204	-0.088	0.514		
10	-0.976	-0.091	-0.809	-0.104	-0.618	-0.272	-0.082	-0.518		
11	-0.964	-0.178	-0.810	0.099	0.955	0.267				
12	-0.970	-0.135	-0.300	-0.820	-0.662	-0.071				
13	-0.979	-0.048	-0.788	-0.229	0.006	0.814				
14	-0.978	0.056	-0.815	-0.049	-0.449	-0.561				
15	-0.973	-0.115	-0.687	0.457						
16	-0.980	-0.033	-0.615	-0.573						
17	-0.974	-0.101								
18	-0.976	-0.073								
19	-0.980	-0.009								
20	-0.979	-0.022								
21	-0.976	-0.060								

Interestingly, very similar trends were obtained in tests where the frequency was varied, and where a shear grazing flow was present. This led us to think that perhaps the set of greedy-selected reflection coefficient values could still be good candidates in drastically different configurations, i.e., that of a 3D engine nacelle (see Sec. V). Re-using pre-selected reflection coefficient values has the advantage to allow to bypass the optimization in Eq. 10, which is quite time consuming for large systems. Prior to considering 3D configurations, an additional validation test case will be performed in Sec. IV.E with a 2D duct geometry in the presence of a shear grazing flow.

C. Link between residual and error

To assert the adequacy of the residual to guide the greedy algorithm, one must make sure that the overall error of the ROM is indeed reduced as the residual decreases too. Here, we define the error ϵ_p as the L_2 norm of the difference between the pressure fields at the wall opposite the liner (subscript w) obtained with ROM and with the HF solver, i.e.,

$$\epsilon_p = \frac{\left\|\tilde{p}_{w,\,\mathrm{ROM}} - \tilde{p}_{w,\,\mathrm{HF}}\right\|_2}{p_{\mathrm{in}}}, \tag{12}$$

where p_{in} is the amplitude of the incident pressure wave. In order to verify the link between error and residual, calls to the HF solver are performed at each element of a fine discrete set $\Xi \subset \mathcal{D}$ containing ≈ 1600 elements, i.e., values of $\tilde{R}$ where the residual is evaluated. The calculation is repeated for different values of m, in the same 2D configuration as the one studied in Sec. IV.B with re $\left(\tilde{Z}\right) \geq 0.5$. The comparison between error ϵ_p and maximum residual $\Delta_p\left(\underline{\underline{V_m}}\right)$ is plotted in Fig. 5, where each marker corresponds to an element of Ξ (representing ≈ 1600 calls to the HF solver for each m).

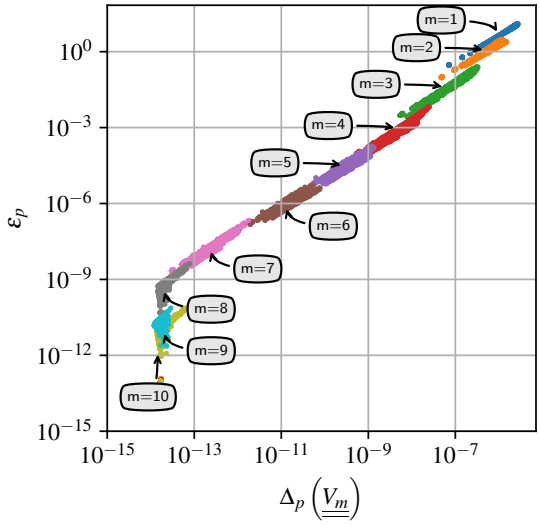

Figure 5 Residual-error relationship for the 2D case of Sec. IV.A, where re $\left(\tilde{Z}\right) \geq 0.5$ and $f = 500$ Hz.

There is a positive correlation and an almost linear relationship between ϵ_p and $\Delta_p\left(\underline{\underline{V_m}}\right)$ up to $m = 8$, which indicates that the use of the residual to control the greedy selection of snapshots is indeed a proper strategy. We estimate that machine precision errors are responsible for the loss of linearity after $m = 8$.

D. Extension to multiple impedances

A common case encountered by liner designers is the simultaneous design of multiple acoustically treated surfaces. It stands to reason to believe that the optimal impedance can be dissimilar between these surfaces. As a result, one has more than one impedance to consider during the building of an impedance map, which drastically increases the number of required calls to a HF solver. In the present section, we evaluate the greedy selection technique when two different impedances are considered. The test case is again that of Sec. IV.A, however the liner is split in two equal length BCs, with reflection coefficients $\tilde{R}_1$ and $\tilde{R}_2$ from left to right respectively in Fig. 1. Convergence results of the greedy algorithm are displayed in Fig. 6 and compared with the regular case with only one impedance surface. As expected, an increase in the size of the parameter space led to a increase in the size required by the RB to reach convergence. Convergence was obtained in less than 30 iterations.

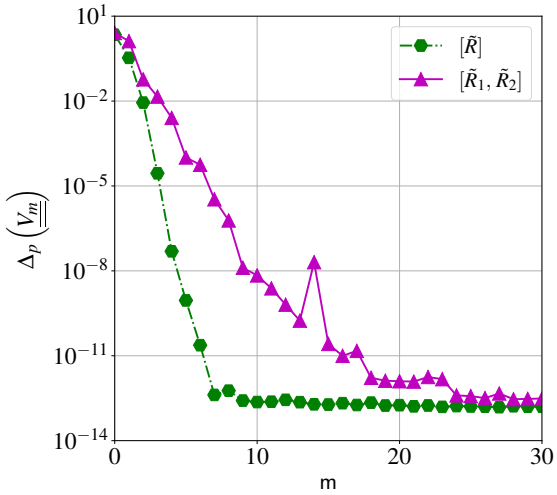

Figure 6 Residual in the case where two impedance surfaces are present, where re $\left(\tilde{Z}\right) \geq 0.5$ and $f = 500\,\mathrm{Hz}$.

The locations of the snapshots are shown for $\tilde{R}_1$ and $\tilde{R}_2$ in the reflection coefficient space in Fig. 7. While the locations seem similar to that obtained in the case where a single impedance was considered (see Fig. 3a), a lot more snapshots are now located near the rigid wall limit $\tilde{R} = 1$, which, at first, contradicts our previous statement on the importance of an impedance discontinuity for the residual convergence. However, it is important to remember here that the values of $\tilde{R}_1$ and $\tilde{R}_2$ displayed in Fig. 7 are obtained by the greedy algorithm in a particular order. In the case where multiple impedance surfaces are present, the greedy algorithm converged towards couple of values that exhibited a high impedance discontinuity in-between the surfaces: this is the case for instance when $\tilde{R}_1 = 1$ and $\tilde{R}_2 = -1/3$, where a high impedance discontinuity is reached at the junction between the impedance surfaces, and also between the second impedance surface and the rigid wall immediately downstream. This observation raises the question as to whether one should also provide an upper limit to re $\left(\tilde{Z}\right)$ when performing this type of optimization, thus reducing the number of calls to rigid configurations, which can be of lesser interest to the liner designer. It is expected that for impedance surfaces well apart from each other, the aforementioned effect be less pronounced, and the convergence faster.

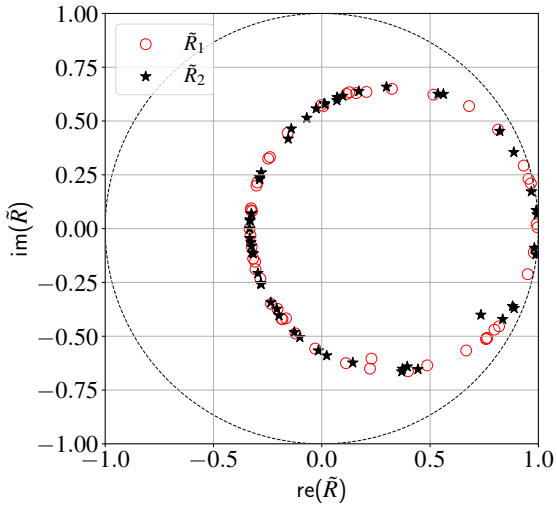

Figure 7 Location of the snapshots in the reflection coefficient space, when 2 impedance surfaces are considered.

E. Validation on a 2D problem with flow

To evaluate the possibility of using the optimally selected snapshot values of Table. 1 in a configuration more complex than that of Sec. IV.A, a comparison between the HF solver and the RB one is made in a 2D case having different features than the one used until now. The considered geometry is that of a duct having a height of $H = 100$ mm, a liner length of 400 mm, and two inlets located on the upper and lower walls, respectively, as shown in Fig. 8. A shear grazing flow of Mach 0.3 at the centerline is accounted for, flowing from right to left, opposed to the main acoustic waves seen the liner. A Poiseuille flow is considered, while not realistic, as it is the least demanding in terms of near-wall meshing (short of considering a uniform flow). Plane waves are imposed on both inlets at a frequency of 2 kHz (was 500 Hz in Sec. IV.A). Due to the orientation of the inlets relatively to the duct and due to the presence of impedance discontinuities, non plane waves are allowed to propagate, as displayed in Fig. 8, making this configuration a priori more challenging than the nominal case studied in Sec. IV.A.

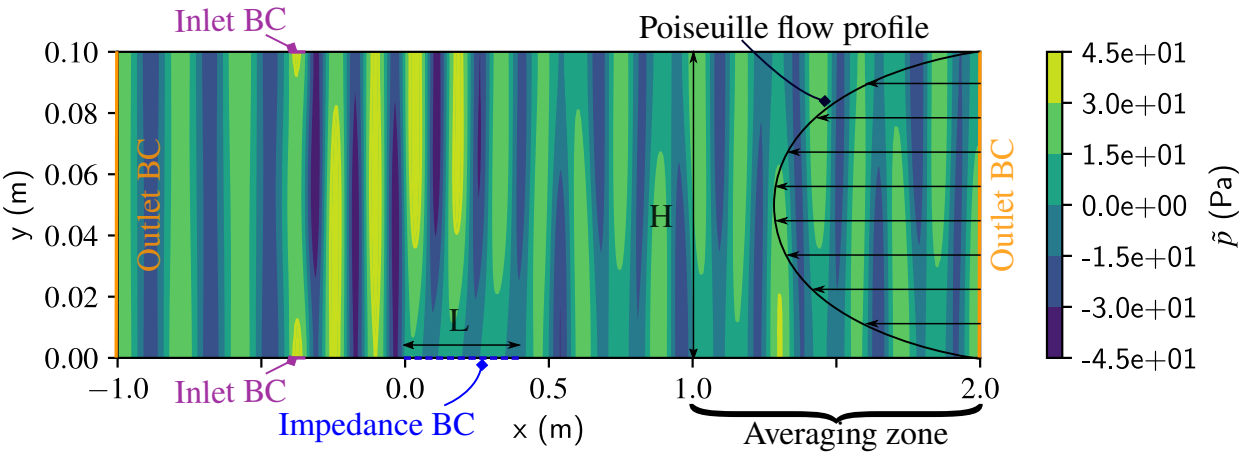

Figure 8 Real part of the pressure field and schematic of the treated 2D duct considered for the extended validation, when $\tilde{Z} = 1$ (not to scale).

A set of 900 different impedance values is considered, uniformly distributed over $\mathrm{re}\left(\tilde{Z}\right) \in [0, 4]$ and $\mathrm{im}\left(\tilde{Z}\right) \in [-4, 4]$. The RB is built using the snapshot values contained in Table 1, in the column corresponding to $\mathrm{re}\left(\tilde{Z}\right) \geq 1$, meaning that the RB size is $m = 7$. This choice is made in order to test the configuration when the threshold resistance is higher than the resistance of interest: is the approximation still correct in complex configurations at low resistance?

The indicator selected for display in this test case is an insertion loss (IL, in dB), evaluated downstream of the liner test section. The IL is the difference between the average SPL when an impedance BC is considered with the average SPL obtained when a wall BC is taken instead. This quantity is interesting in aeroacoustics, as minimizing it is key to the efficient design of liners. The SPL average is evaluated over a length of 1 m, as indicated in Fig. 8, which corresponds to almost 12 wave-lengths. The ILs obtained for both solvers are displayed in Fig. 9.

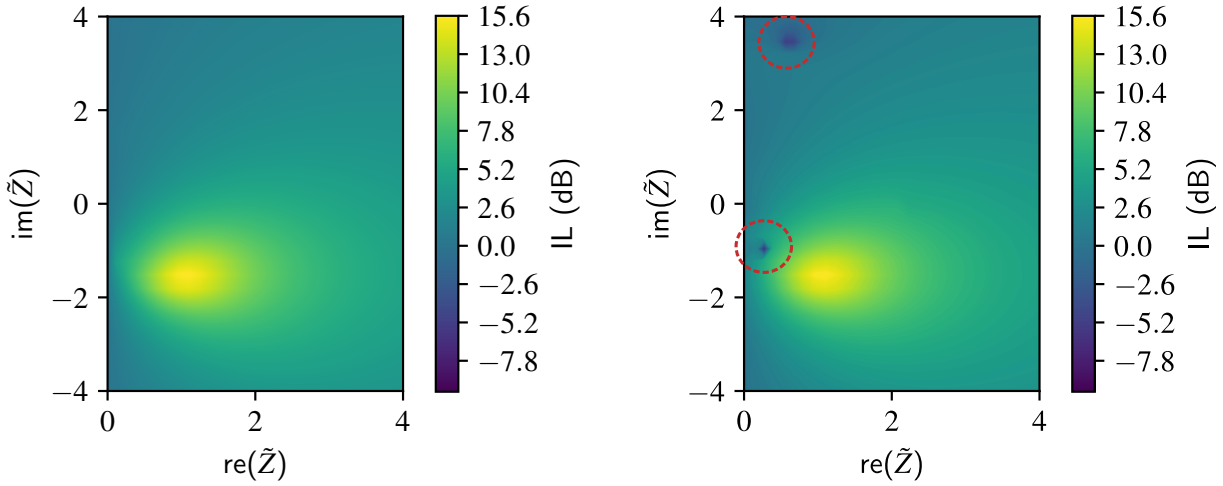

(a) IL, HF solver

(b) IL, RB solver where the snapshots had to respect re $\left(\tilde{Z}\right) \geq 1$. Circled areas correspond to outliers with a clear mismatch with the HF solver.

Figure 9 Comparison between the ILs obtained with the HF and RB solvers on the extended 2D duct test case.

While the obtained ILs look very much alike, some discrepancies are obtained. Negative values of the IL, which are only present in Fig. 9b for the RB solver, indicate a gain of energy in the system (the SPL is higher after the liner than it would be with a rigid wall), which is unphysical. Apart from these two calculations (out of 900), circle in Fig. 9b, the approximation error is quite low. It is worthwhile to note that despite using the snapshots optimized with the resistance threshold re $\left(\tilde{Z}\right) \geq 1$, the RB solver can still be accurate for re $\left(\tilde{Z}\right) < 1$. To further investigate the disparity between solvers, an error index is created as

$$\epsilon_{\text{IL}} = |\text{IL}_{\text{HF}} - \text{IL}_{\text{RB}}| \,. \tag{13}$$

This error index represents the direct mismatch between solvers, and is quite small at almost every tested impedances. The log of this error is represented in Fig. 10, along with the log of the average pressure residual, which is averaged in the same zone as the IL. Even in this extended duct configuration, the residual proves to be an excellent a posteriori error indicator. If one were interested in the IL at an impedance value where the residual is high, one would need to perform another call to the HF solver and extend the RB using the approach described in Eq. 11.

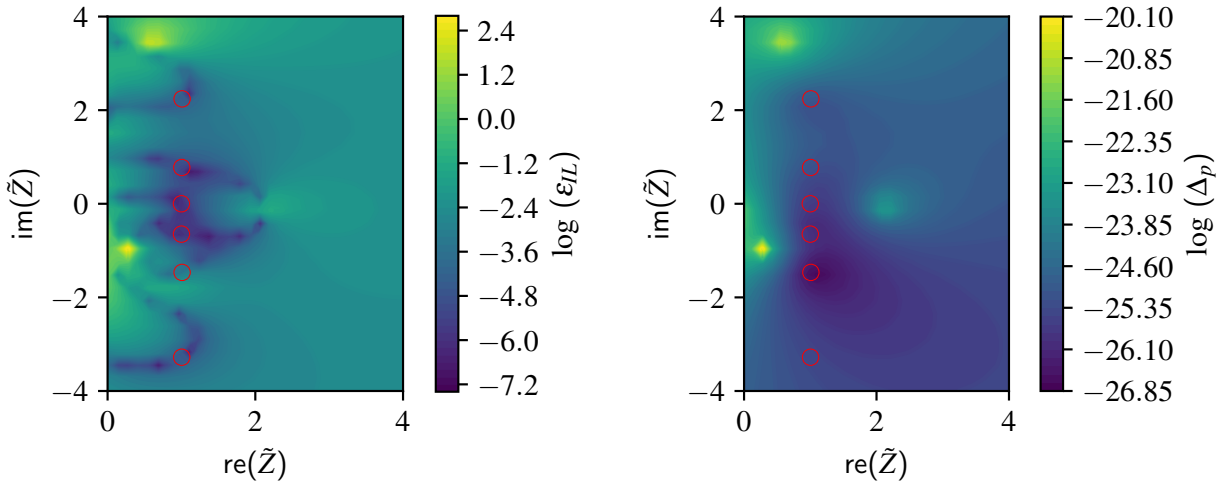

(a) Log of the error index

(b) Log of the pressure residual

Figure 10 Error and pressure residual obtained with the RB solver on the extended 2D duct test case, with the snapshots corresponding to the column re $\left(\tilde{Z}\right) \geq 1$ in Table 1. The red circles mark the location of snapshots contained within the bounds of the considered impedances. One of the snapshots ($\tilde{Z} = \infty$ associated to $\tilde{R} = 1$) is outside the bounds.

V. Extension to a 3D case with flow

A. 3D nacelle engine

The results of the previous sections are now used for the exploration of the impedance space associated with a 3D engine nacelle configuration. An additional equation for the third component of velocity is present in the LEE, thus extending Eq. 2. The mesh considered in this work is displayed in Fig. 11a and a schematic is presented in Fig. 11b, where the different boundary conditions are made explicit. The liner is about 1.16 m long, while the nacelle has an internal diameter of about 3 m.

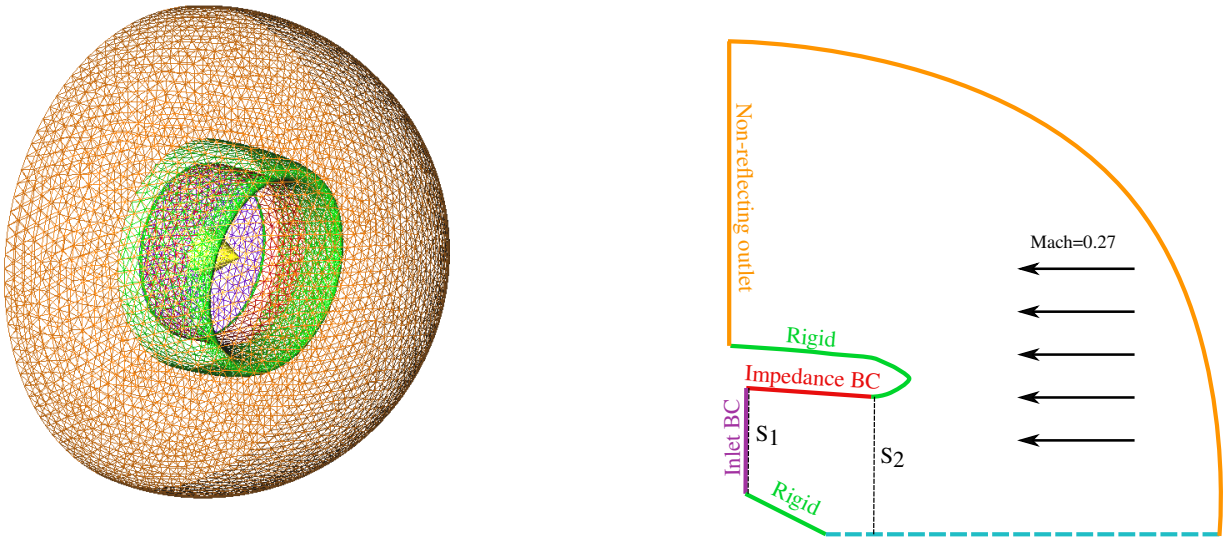

(a) Full mesh.

(b) Boundary conditions (not to scale).

Figure 11 3D nacelle configuration.

Using previous knowledge on acoustic liners placed in aeroengines, the minimum value of resistance is fixed to 0.5 in the greedy selection algorithm (allowing the use of the corresponding column in Table 1). This choice is motivated by the presence of a strong shear grazing flow and SPL in such nacelles, which results in an increase in the resistance. Note that the previous hypothesis does not necessarily preclude precise solutions to be reached for re $\left(\tilde{Z}\right) < 0.5$. A mean flow solution was first calculated using a dedicated flow solver, and then projected onto the DG mesh. The inlet mean flow Mach number was around 0.27, flowing from right to left as represented in Fig. 11b.

Only a single frequency is considered ($f = 587\,\text{Hz}$), and the inlet condition consists in a high order acoustic mode (radial order 0, azimuthal order 4), different from the plane wave mode used so far. Once the ROM is built, the quantity of interest can be evaluated at all impedance values of interest, thus generating a map. Here, the observed acoustic quantity is an attenuation coefficient α (in dB), defined using the acoustic intensity at surfaces before and after the liner, respectively S_1 and S_2 in Fig. 11b, as

$$\alpha = -10 \log_{10} \left| \frac{\oint_{S_2} \boldsymbol{i} \cdot \mathrm{d}\boldsymbol{S}}{\oint_{S_1} \boldsymbol{i} \cdot \mathrm{d}\boldsymbol{S}} \right|. \tag{14}$$

The intensity $\boldsymbol{i}$ (in $\mathrm{W/m^2}$) is defined by Cantrell and Hart [43] as

$$\boldsymbol{i} = \tilde{p}\tilde{\boldsymbol{u}} + \frac{\tilde{p}^2}{\rho_0 c_0^2}\tilde{\boldsymbol{u}} + \rho_0 \left(\boldsymbol{u_0} \cdot \tilde{\boldsymbol{u}}\right) \tilde{\boldsymbol{u}} + \frac{\tilde{p}}{c_0^2} \left(\boldsymbol{u_0} \cdot \tilde{\boldsymbol{u}}\right) \boldsymbol{u_0}, \tag{15}$$

where $\tilde{\boldsymbol{u}} = [\tilde{u}, \tilde{v}, \tilde{w}]$ and $\boldsymbol{u_0} = [U_0, V_0, W_0]$, with $\tilde{w}$ and W_0 the acoustic and mean flow velocities in the transverse direction. A few calls to the HF solver were made at different impedance values to validate the precision of the reduced basis, showing an excellent agreement. However, due to the numerical budget required for each full calculation, the total attenuation coefficient map was not evaluated. In this 3D configuration, the size of the initial problem is $N \approx 10^6$ and the HF solver is run on 1024 processors in $\approx 3\,\text{min}$.

The impedance map of the attenuation coefficient is obtained using the greedy algorithm with $m = 10$, as per Table 1. The attenuation coefficient map is displayed in Fig. 12, and consists in the interpolation of 2821 values of α obtained with the RB. Each value of α was obtained in less than 0.3 s, which includes calculating the solution (Eqs. 6, 7), and extracting and saving on disk the attenuation calculation. Calculating the approximated solution only took $\approx 0.15\,\text{ms}$, meaning that the problem is now dominated by the postprocessing (and the initial snapshot calculations).

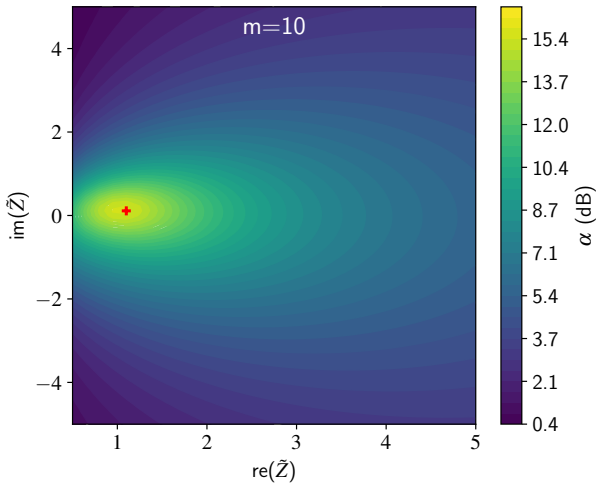

Figure 12 Impedance map of the attenuation coefficient. The red cross marks the optimal value.

From the map in Fig. 12, one deduces the optimal impedance $\tilde{Z}_{\text{opt}} \approx 1.1 + 0.11\text{j}$. The difference between the intensity fields of a rigid case (where the impedance is $\tilde{Z}_{\text{rigid}} = +\infty$) and a lined (not optimal) case is displayed in Fig. 13.

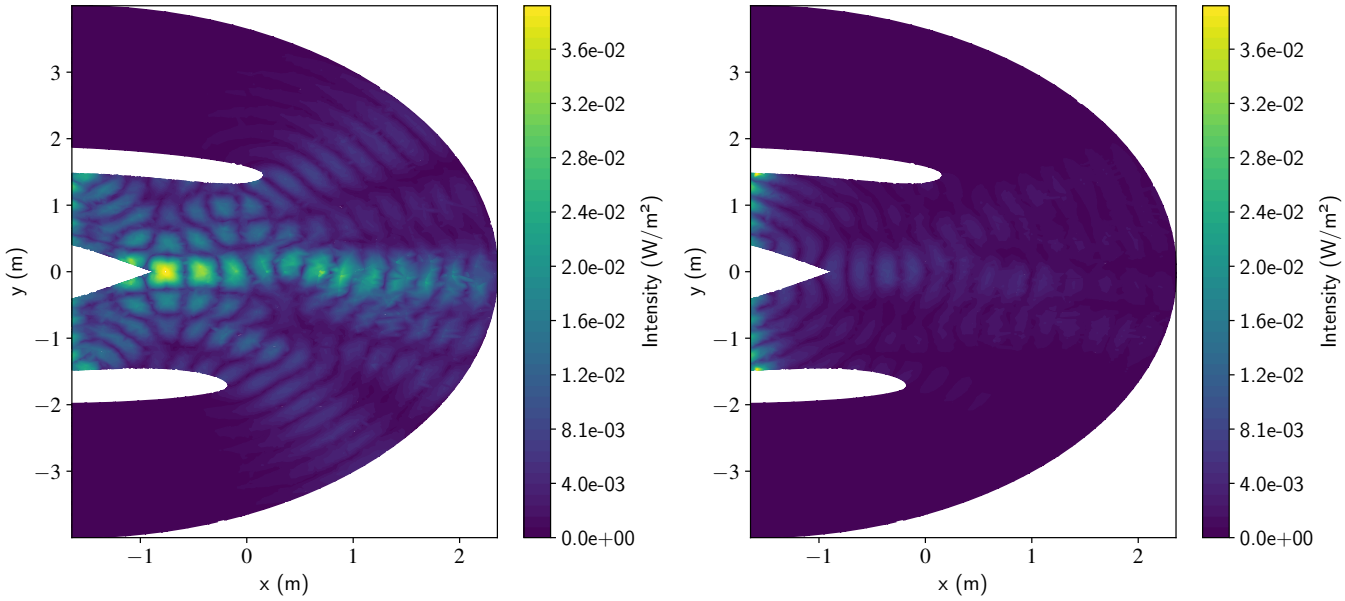

(a) Rigid

(b) Lined

Figure 13 Absolute value of the intensity field.

In order to test the convergence of the ROM as a function of the available numerical budget, different values of m were selected. Comparisons between the different cases ($m \in [2, 9]$) are shown in Fig. 14, displaying the difference Δ_α of the impedance maps of the acoustic indicator with respect to the solution for $m = 10$, i.e.,

$$\Delta_\alpha = |\alpha\,(i) - \alpha\,(m = 10)|\,, \quad i \in [2, 9]. \tag{16}$$

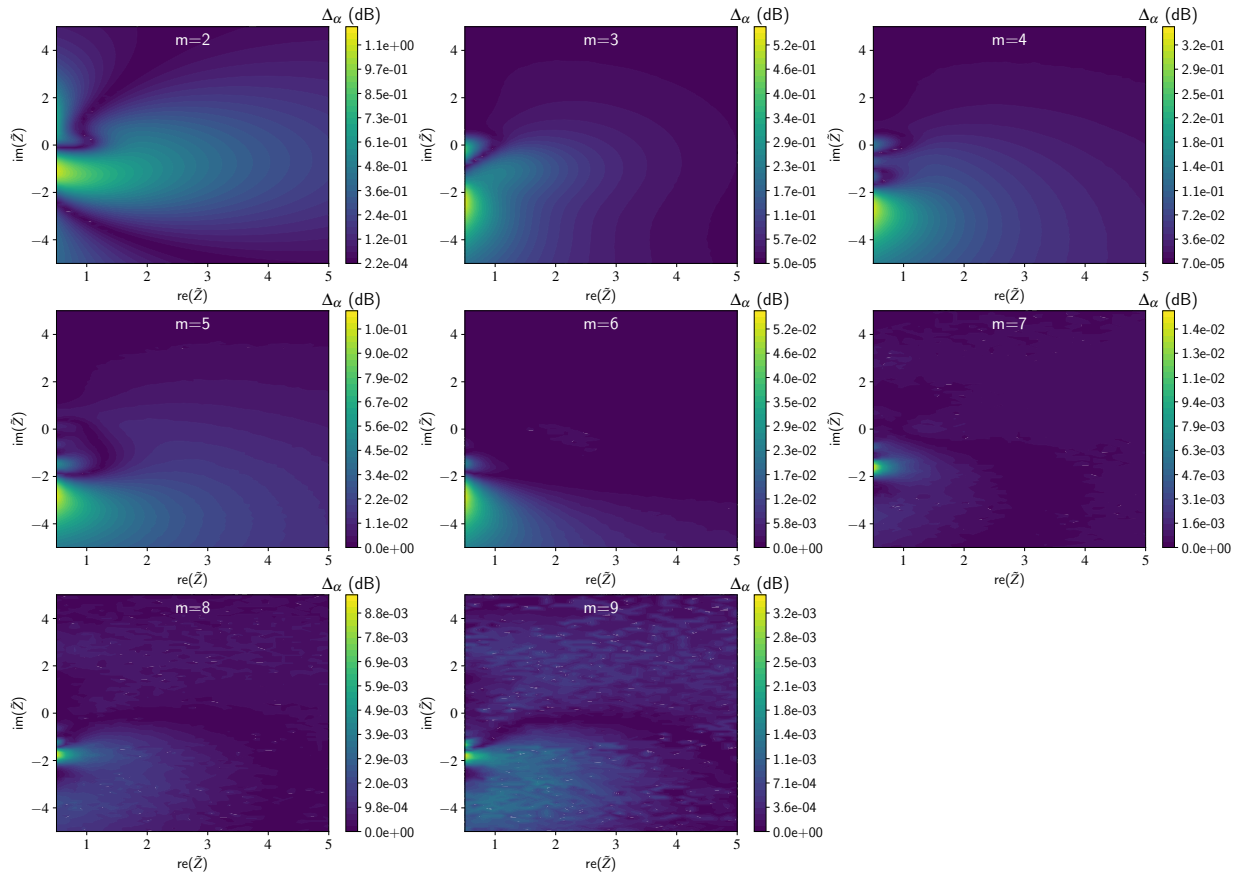

Figure 14 Difference of the impedance map of the attenuation coefficient with respect to the case $m = 10$.

As expected, high values of Δ_α are concentrated towards the limit $\mathrm{re}\left(\tilde{Z}\right) = 0.5$, where the maximum of impedance discontinuity is realized. However, it is shown that for as little as $m = 3$, the error made on the map is relatively small (2%) with respect to the maximum of attenuation of 16 dB. The averaged L_2 difference $\overline{\Delta_\alpha^2}$ made on these maps is obtained on the fine discrete set $\Xi \subset \mathcal{D}$ and is given by

$$\overline{\Delta_\alpha^2} = \frac{1}{N_\Xi} \sum_{\tilde{R} \in \Xi} \Delta_\alpha^2 \left(\tilde{R}\right), \tag{17}$$

here with $N_\Xi \approx 2.8 \cdot 10^3$ the number of elements in Ξ. The $\overline{\Delta_\alpha^2}$ quantity is shown in Fig. 15. A quasi exponential convergence of the average error $\overline{\Delta_\alpha^2}$ is observed as a function of m, indicating the correctness of the chosen values of reflection coefficients. It is remarkable that for a widely different case that the one where the reflection coefficient values were optimized for, the created RB remains exploitable. Further work needs to be pursued in order to verify whether the values in Table. 1 are universal enough to be used in any aeroacoustic problem, including ones where the linearized Navier-Stokes equations are considered.

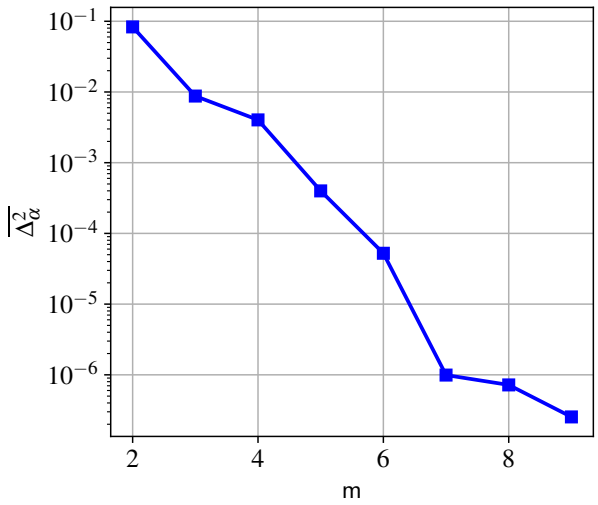

Figure 15 Average quadratic error of the impedance map of the acoustic indicator with respect to the case $m = 10$.

B. Discussion on the speed-up factors

When using a snapshot based ROM, defining a speed-up factor can be tricky. Clearly, once the ROM is built, assembling the reduced system Eq. 6 at a given impedance value takes about $O\left(m^2\right)$ operations and inverting the system requires about $O\left(m^3\right)$ operations using a direct solver. Expressing the RB solution in the DG basis using Eq. 7 amounts to $O\left(mN\right)$ operations. Thus, in the limit $m \ll N$, the cost of the RB solution at a given impedance value requires roughly $O\left(mN\right)$ operations. This is incomparably cheap compared to the HF solver, which requires not only the assembly of a large-scale $N \times N$ sparse linear system, but also its iterative resolution (here, we rely on the FETI-2LM method [44]). As in the ROM literature [45, 46], the speed-up is evaluated here as the ratio between the elapsed time for solving the ROM and the elapsed time for solving the HF problem. This omits the costs associated to the construction of the ROM, which is dominated by the m HF solutions. In the 2D case presented in Sec. IV.A, the speed-up factor was 10^3, while it was $\approx 10^4$ in the more complex 2D case of Sec. IV.E. In the 3D nacelle case of Sec. V, the speed-up factor reached $\approx 1.2 \cdot 10^6$. Note that in practice, one needs to extract part of the solution in order to evaluate the quantity of interest, and some of the solution needs to be saved on disk. These operations were, in the present case, dominating the numerical cost of the 3D case, bringing back the speed-up factor to $\approx 6 \cdot 10^2$.

VI. Conclusion

An optimal set of reflection coefficient values (or equivalently, of impedance values) was obtained in order to build a reduced basis. The time-harmonic linearized Euler equations, once projected onto this basis, yield a linear system for the harmonic problem that is orders of magnitude faster to solve, thus enabling the fast exploration of solutions where the impedance is varied. The optimal building of this reduced basis is obtained via a greedy algorithm, based on the residual, and avoids the use of a proper orthogonal decomposition.

The greedy selection technique was first applied on a 2D geometry of a duct, equipped with an acoustic liner, represented by an impedance boundary condition. It was discovered that when the real part of the impedance (the resistance) was known to be above a certain value, the resulting reduced basis would need fewer elements to represent the system, and thus fewer calls to the high-fidelity solver. This phenomenon is caused by the impedance discontinuity. This lower limit of the resistance is consistent with the impedance models related to the presence of a shear grazing flow or a high sound pressure level. Different sets of reflection coefficient values were given for different minimal values of the resistance, for future users to select with respect to their own liner specifications. In order to evaluate the robustness of the method, the same set of values were used in a different 2D duct geometry, in the presence of a shear grazing flow of centerline Mach of 0.3, with non-plane waves at a frequency four times the one considered previously. The resulting reduced basis was favorably compared against the high fidelity solver, displaying a good fit between the insertion loss

evaluated by both solvers.

The 3D geometry of a nacelle was considered at yet a different frequency, in the presence of a shear grazing flow, and with a higher order acoustic mode than for the 2D configuration. It was shown that with as little as 3 full high-fidelity resolutions of the linearized Euler equations, one was then able to recover a precise mapping of the acoustic indicator, here an attenuation coefficient. The initial speed-up factor for the 3D case was $\approx 1.2 \cdot 10^6$, and was then brought back to $\approx 6 \cdot 10^2$ due to the evaluation and saving on disk of the quantity of interest.

It is expected that this work could benefit liner designers and aeroacousticians dealing with impedance eduction problems, leading to faster initial evaluation of designs, and faster impedance eductions. Compared with our initial work in Ref. [13], the present work introduces a technique capable of drastically reducing the number of calls to the high-fidelity solver to create an efficient reduced basis, which could render possible the routine use of 3D configurations for liner eduction and optimisations. The immediate next step to consider is the introduction of a viscosity term in the equations, by adopting a linearized Navier-Stokes formalism.

References

[1] Casalino, D., Diozzi, F., Sannino, R., and Paonessa, A., "Aircraft noise reduction technologies: a bibliographic review," *Aerosp. Sci. Technol.*, Vol. 12, No. 1, 2008, pp. 1–17. https://doi.org/10.1016/j.ast.2007.10.004.

[2] Hooper, P. D., Thomas, C. S., Hume, K. I., and Maughan, J. A., "Aircraft Noise: Alleviating Constraints to Airport Operations and Growth," *Green Aviation*, 2016, p. 267. https://doi.org/10.1002/9780470686652.eae343.pub2.

[3] Mery, F., Roncen, R., Simon, F., Ostorero, L., and Botte, M., "Design, manufacturing and experimental assessment of an acoustic liner demonstrator for a turning vane of S1MA large wind tunnel facility," *28th AIAA/CEAS Aeroacoustics 2022 Conference*, Southampton, UK, 2022, p. 2855. https://doi.org/10.2514/6.2022-2855.

[4] Jones, M. G., Simon, F., and Roncen, R., "Broadband and Low-Frequency Acoustic Liner Investigations at NASA and ONERA," *AIAA Journal*, 2021, pp. 1–20. https://doi.org/10.2514/1.J060862.

[5] Maa, D.-Y., "Theory and design of microperforated panel sound-absorbing constructions," *Sci. Sin.*, Vol. 18, No. 1, 1975, pp. 55–71. https://doi.org/10.1360/ya1975-18-1-55.

[6] Atalla, N., and Sgard, F., "Modeling of perforated plates and screens using rigid frame porous models," *J. Sound Vib.*, Vol. 303, No. 1-2, 2007, pp. 195–208. https://doi.org/10.1016/j.jsv.2007.01.012.

[7] Watson, W., Jones, M., and Parrott, T., "Validation of an impedance eduction method in flow," *AIAA journal*, Vol. 37, No. 7, 1999, pp. 818–824. https://doi.org/10.2514/2.7529.

[8] Jones, M. G., Watson, W. R., and Parrott, T. L., "Benchmark data for evaluation of aeroacoustic propagation codes with grazing flow," *AIAA paper*, Vol. 2853, 2005, p. 2005. https://doi.org/10.2514/6.2005-2853.

[9] Eversman, W., and Gallman, J. M., "Impedance eduction with an extended search procedure," *AIAA journal*, Vol. 49, No. 9, 2011, pp. 1960–1970. https://doi.org/10.2514/1.J050831.

[10] Busse-Gerstengarbe, S., Richter, C., Thiele, F. H., Lahiri, C., Enghardt, L., Roehle, I., Ferrante, P., and Scofano, A., "Impedance eduction based on microphone measurements of liners under grazing flow conditions," *AIAA journal*, Vol. 50, No. 4, 2012, pp. 867–879. https://doi.org/10.2514/1.J051232.

[11] Primus, J., Piot, E., and Simon, F., "An adjoint-based method for liner impedance eduction: Validation and numerical investigation," *J. Sound Vib.*, Vol. 332, No. 1, 2013, pp. 58–75. https://doi.org/10.1016/j.jsv.2012.07.051.

[12] Zhou, L., and Boden, H., "A systematic uncertainty analysis for liner impedance eduction technology," *J. Sound Vib.*, , No. 356, 2015, pp. 86–99. https://doi.org/10.1016/j.jsv.2015.07.001.

[13] Roncen, R., Méry, F., Piot, E., and Simon, F., "Statistical Inference Method for Liner Impedance Eduction with a Shear Grazing Flow," *AIAA Journal*, 2018, pp. 1–11. https://doi.org/10.2514/1.J057559.

[14] Lafont, V., Méry, F., Roncen, R., Simon, F., and Piot, E., "Liner Impedance Eduction Under Shear Grazing Flow at a High Sound Pressure Level," *AIAA Journal*, Vol. 58, No. 3, 2020, pp. 1107–1117. https://doi.org/10.2514/1.J058756.

[15] Guess, A., "Calculation of perforated plate liner parameters from specified acoustic resistance and reactance," *J. Sound Vib.*, Vol. 40, No. 1, 1975, pp. 119–137. https://doi.org/10.1016/S0022-460X(75)80234-3.

[16] Kirby, R., and Cummings, A., "The impedance of perforated plates subjected to grazing gas flow and backed by porous media," *J. Sound Vib.*, Vol. 217, No. 4, 1998, pp. 619–636. https://doi.org/10.1006/jsvi.1998.1811.

[17] Chen, Z., Ji, Z., and Huang, H., "Acoustic impedance of perforated plates in the presence of fully developed grazing flow," *J. Sound Vib.*, Vol. 485, 2020, p. 115547. https://doi.org/10.1016/j.jsv.2020.115547.

[18] Melling, T. H., "The acoustic impendance of perforates at medium and high sound pressure levels," *J. Sound Vib.*, Vol. 29, No. 1, 1973, pp. 1–65. https://doi.org/10.1016/S0022-460X(73)80125-7.

[19] Temiz, M. A., Tournadre, J., Arteaga, I. L., and Hirschberg, A., "Non-linear acoustic transfer impedance of micro-perforated plates with circular orifices," *J. Sound Vib.*, Vol. 366, 2016, pp. 418–428. https://doi.org/10.1016/j.jsv.2015.12.022.

[20] Renou, Y., and Aurégan, Y., "Failure of the Ingard–Myers boundary condition for a lined duct: An experimental investigation," *J. Acoust. Soc. Am.*, Vol. 130, No. 1, 2011, pp. 52–60. https://doi.org/10.1121/1.3586789.

[21] Bodén, H., Cordioli, J. A., and Spillere, A. M., "Effect of flow direction on acoustic liner impedance measurement results," *23rd International Congress on Sound and Vibration, ICSV 2016, 10 July 2016 through 14 July 2016*, 2016.

[22] Bodén, H., Cordioli, J. A., Spillere, A., and Serrano, P., "Comparison of the effect of flow direction on liner impedance using different measurement methods," *23rd AIAA/CEAS Aeroacoustics Conference*, 2017, p. 3184. https://doi.org/10.2514/6.2017-3184.

[23] Weng, C., Schulz, A., Ronneberger, D., Enghardt, L., and Bake, F., "Flow and viscous effects on impedance eduction," *AIAA Journal*, Vol. 56, No. 3, 2017, pp. 1118–1132. https://doi.org/10.2514/1.J055838.

[24] Schulz, A., Weng, C., Bake, F., Enghardt, L., and Ronneberger, D., "Modeling of liner impedance with grazing shear flow using a new momentum transfer boundary condition," *23rd AIAA/CEAS Aeroacoustics Conference*, Denver, Colorado, USA, 2017, p. 3377. https://doi.org/10.2514/6.2017-3377.

[25] Roncen, R., Piot, E., Mery, F., Simon, F., Jones, M. G., and Nark, D. M., "Influence of Source Propagation Direction and Shear Flow Profile in Impedance Eduction of Acoustic Liners," *25th AIAA/CEAS Aeroacoustics Conference*, 2019, p. 2469. https://doi.org/10.2514/6.2019-2469.

[26] Schilders, W., "Introduction to model order reduction," *Model order reduction: theory, research aspects and applications*, Springer, Berlin, Germany, 2008, pp. 3–32. https://doi.org/10.1007/978-3-540-78841-6_1.

[27] Rozza, G., Huynh, D. B. P., and Patera, A. T., "Reduced basis approximation and a posteriori error estimation for affinely parametrized elliptic coercive partial differential equations," *Arch. Comput. Methods Eng.*, Vol. 15, No. 3, 2008, pp. 229–275. https://doi.org/10.1007/s11831-008-9019-9.

[28] Veroy, K., Prud'Homme, C., Rovas, D., and Patera, A., "A posteriori error bounds for reduced-basis approximation of parametrized noncoercive and nonlinear elliptic partial differential equations," *16th AIAA Computational Fluid Dynamics Conference 2003*, American Institute of Aeronautics and Astronautics Inc.(AIAA), 2003. https://doi.org/10.2514/6.2003-3847.

[29] Huynh, D. P., Knezevic, D. J., Peterson, J. W., and Patera, A. T., "High-fidelity real-time simulation on deployed platforms," *Computers & Fluids*, Vol. 43, No. 1, 2011, pp. 74–81. https://doi.org/10.1016/j.compfluid.2010.07.007.

[30] Binev, P., Cohen, A., Dahmen, W., DeVore, R., Petrova, G., and Wojtaszczyk, P., "Convergence rates for greedy algorithms in reduced basis methods," *SIAM J. Math. Anal.*, Vol. 43, No. 3, 2011, pp. 1457–1472. https://doi.org/10.1137/100795772.

[31] Buffa, A., Maday, Y., Patera, A. T., Prud'homme, C., and Turinici, G., "A priori convergence of the greedy algorithm for the parametrized reduced basis method," *ESAIM: Math. Model. Numer. Anal.*, Vol. 46, No. 3, 2012, pp. 595–603. https://doi.org/10.1051/m2an/2011056.

[32] Geuzaine, C., and Remacle, J.-F., "Gmsh: A 3-D finite element mesh generator with built-in pre-and post-processing facilities," *Int. J. Num. Meth. Engng*, Vol. 79, No. 11, 2009, pp. 1309–1331. https://doi.org/10.1002/nme.2579.

[33] Monteghetti, F., Matignon, D., Piot, E., and Pascal, L., "Design of broadband time-domain impedance boundary conditions using the oscillatory-diffusive representation of acoustical models," *J. Acoust. Soc. Am.*, Vol. 140, No. 3, 2016, pp. 1663–1674. https://doi.org/10.1121/1.4962277.

[34] Fiévet, R., Deniau, H., and Piot, E., "Strong compact formalism for characteristic boundary conditions with discontinuous spectral methods," *J. Comput. Phys.*, Vol. 408, 2020, p. 109276. https://doi.org/10.1016/j.jcp.2020.109276.

[35] Delorme, P., Mazet, P.-A., Peyret, C., and Ventribout, Y., "Computational Aeroacoustics Applications based on a Discontinuous Galerkin Method," *Comptes rendus de l'Académie des sciences - Serie IIb - Mécanique/Mechanics*, Vol. 333, 2005, pp. 676–682.

[36] Peyret, C., and Delorme, P., "Optimal hp Discontinuous Galerkin Method, Application to Computational Aeroacoustics," *11th AIAA/CEAS Aeroacoustics Conference*, 2005. https://doi.org/10.2514/6.2005-2822.

[37] Pascal, L., Piot, E., and Casalis, G., "Discontinuous Galerkin method for the computation of acoustic modes in lined flow ducts with rigid splices," *J. Sound Vib.*, Vol. 332, No. 13, 2013, pp. 3270 – 3288. https://doi.org/10.1016/j.jsv.2013.01.021.

[38] Ventribout, Y., and Mazet, P.-A., "Contrôle d'onde acoustique par impédance de paroi," *Congrès d'Analyse Numérique (Canum 2003)*, 2003.

[39] Hesthaven, J. S., and Warburton, T., *Nodal discontinuous Galerkin methods: algorithms, analysis, and applications*, Springer Science & Business Media, New York, 2007. https://doi.org/10.1007/978-0-387-72067-8.

[40] Pinnau, R., "Model reduction via Proper Orthogonal Decomposition," *Model order reduction: theory, research aspects and applications*, Vol. 13, Springer, Berlin, Heidelberg, Berlin, Germany, 2008, pp. 95–109. https://doi.org/10.1007/978-3-540-78841-6_5.

[41] Blank, J., and Deb, K., "Pymoo: Multi-Objective Optimization in Python," *IEEE Access*, Vol. 8, 2020, pp. 89497–89509. https://doi.org/10.1109/ACCESS.2020.2990567.

[42] Roncen, R., Edel, P., and Peyret, C., "Optimal selection of snapshots in the Reduced Basis Method for linearized aeroacoustic with impedance boundary conditions," *28th AIAA/CEAS Aeroacoustics 2022 Conference*, 2022, p. 2901. https://doi.org/10.2514/6.2022-2901.

[43] Cantrell, R., and Hart, R., "Interaction between sound and flow in acoustic cavities: Mass, momentum, and energy considerations," *J. Acoust. Soc*, Vol. 36, No. 4, 1964, pp. 697–706. https://doi.org/10.1121/1.1919047.

[44] Farhat, C., Macedo, A., Lesoinne, M., Roux, F.-X., Magoulés, F., and de La Bourdonnaie, A., "Two-level domain decomposition methods with Lagrange multipliers for the fast iterative solution of acoustic scattering problems," *Comput Methods Appl Mech Eng*, Vol. 184, No. 2-4, 2000, pp. 213–239. https://doi.org/10.1016/S0045-7825(99)00229-7.

[45] Manzoni, A., Quarteroni, A., and Rozza, G., "Model reduction techniques for fast blood flow simulation in parametrized geometries," *Int J Numer Method Biomed Eng*, Vol. 28, No. 6-7, 2012, pp. 604–625. https://doi.org/10.1002/cnm.1465.

[46] Manzoni, A., Quarteroni, A., and Rozza, G., "Shape optimization for viscous flows by reduced basis methods and free-form deformation," *Int. J. Numer. Methods Fluids*, Vol. 70, No. 5, 2012, pp. 646–670. https://doi.org/10.1002/fld.2712.

Acknowledgment

The authors are grateful to the Airbus group for providing, within the scope of the Ambiance project, the nacelle geometry, mesh and flow profile used in Sec. V.